

Vibrational Stark Effect Spectroscopy at the Interface of Ras and Rap1A Bound to the Ras Binding Domain of RalGDS Reveals an Electrostatic Mechanism for Protein–Protein Interaction

Amy J. Stafford, Daniel L. Ensign, and Lauren J. Webb*

Department of Chemistry and Biochemistry and Institute for Cell and Molecular Biology, The University of Texas at Austin, 1 University Station, A5300, Austin, Texas 78712, United States

Received: July 26, 2010; Revised Manuscript Received: September 14, 2010

Electrostatic fields at the interface of the Ras binding domain of the protein Ral guanine nucleotide dissociation stimulator (RalGDS) with the structurally analogous GTPases Ras and Rap1A were measured with vibrational Stark effect (VSE) spectroscopy. Eleven residues on the surface of RalGDS that participate in this protein–protein interaction were systematically mutated to cysteine and subsequently converted to cyano-cysteine in order to introduce a nitrile VSE probe in the form of the thiocyanate (SCN) functional group. The measured SCN absorption energy on the monomeric protein was compared with solvent-accessible surface area (SASA) calculations and solutions to the Poisson–Boltzmann equation using Boltzmann-weighted structural snapshots from molecular dynamics simulations. We found a weak negative correlation between SASA and measured absorption energy, indicating that water exposure of protein surface amino acids can be estimated from experimental measurement of the magnitude of the thiocyanate absorption energy. We found no correlation between calculated field and measured absorption energy. These results highlight the complex structural and electrostatic nature of the protein–water interface. The SCN-labeled RalGDS was incubated with either wild-type Ras or wild-type Rap1A, and the formation of the docked complex was confirmed by measurement of the dissociation constant of the interaction. The change in absorption energy of the thiocyanate functional group due to complex formation was related to the change in electrostatic field experienced by the nitrile functional group when the protein–protein interface forms. At some locations, the nitrile experiences the same shift in field when bound to Ras and Rap1A, but at others, the change in field is dramatically different. These differences identify residues on the surface of RalGDS that direct the specificity of RalGDS binding to its *in vivo* binding partner, Rap1A, through an electrostatic mechanism.

Introduction

Understanding the physical mechanisms that govern the association of two or more proteins into a functioning complex is a challenging problem. Protein–protein interactions are caused almost exclusively by noncovalent interactions, such as shape complementarity and electrostatic fields, and are difficult to study in quantitative detail. Because of the vast number of potential protein–protein interactions, there is great interest in developing computational models for predicting both naturally occurring protein–protein interactions and the effect of small molecules on protein–protein interfaces.^{1–8} The accuracy of these models must be verified by experimental measurements of the physical forces that promote a stable and functional protein–protein interface. A growing database of crystal structures of two or more bound proteins has revealed wide diversity in the size, shape, and composition of naturally occurring protein–protein interfaces that cannot be explained through a simplistic charge balance or residue identity.^{9–21} However, it is currently not possible to measure experimentally the electrostatic contributions to interface formation.

The arrangement of amino acid charges from secondary and tertiary protein structure can generate large and heterogeneous electrostatic fields that effect all protein function, including protein–protein interactions.^{22–27} Until recently, local electro-

static fields have been difficult to measure directly, and estimates of electrostatic field strength instead relied on indirect methods, such as determining pK_a values through NMR titration or other techniques.^{28–36} The measurement of pK_a is particularly problematic because of the possibility of pH-dependent structural perturbations.³⁷ For this reason, it has been difficult to validate calculations of detailed, spatially resolved electrostatic potentials, such as those derived from solutions of the Poisson–Boltzmann equation or from full knowledge of the charge density from quantum mechanics.^{38,39} Instead, workers calculating electrostatic properties have usually focused on comparisons to global measurements, such as free energies of binding.^{23,24,40,41} Experimental confirmation of spatially resolved electric fields from calculations is a long-standing biophysical challenge with important implications for understanding biological molecules.^{42–45}

Vibrational Stark effect (VSE) spectroscopy is a recently developed experimental technique capable of measuring electrostatic fields in proteins directly.^{38,39,46–49} In VSE spectroscopy, the intrinsic response of a probe vibrational oscillator to its local electrostatic environment is measured spectroscopically and is used to quantitate the magnitude and direction of the local electric field to which the probe is exposed. After calibration, the probe is inserted into a known position of a protein, where it becomes a highly local, sensitive, and directional reporter of fluctuations of the protein's electrostatic field caused by structural or chemical perturbations to the protein. For example, the formation of a protein–protein interface through a docking

* To whom correspondence should be addressed. E-mail: lwebb@cm.utexas.edu.

interaction may induce changes in the absorption energy of a probe located on each protein surface as that probe is exchanged from an electrostatic field caused by water to one created by the protein–protein interface.

Several useful VSE probes have been identified,⁴⁹ including the nitrile stretching vibration. This oscillator is particularly attractive because its absorption energy, $\sim 2100\text{--}2250\text{ cm}^{-1}$, is in a region of the spectrum that is outside the vibrational background of a complex biomolecule and can be incorporated into proteins with relative ease. It has been established (1) that a single nitrile oscillation can be spectroscopically isolated from the background of a complex protein vibrational absorption spectrum;³⁹ (2) that a general, covalently bound probe like the nitrile can measure changes in electrostatic field on the order of at least 10 MV/cm, which have long been hypothesized to be present in a protein;³⁹ and (3) that isotopic labeling with ^{13}C and ^{15}N on the nitrile bond allows multiple VSE probes to be spectroscopically resolved in a single absorption measurement,⁴⁸ thus allowing a protein electrostatic field to be measured simultaneously from two or more locations. VSE spectroscopy has been used to examine electrostatic fields of enzyme active sites.^{39,50} Nitriles have also been used as spectroscopic probes in simple protein^{38,39,48,51–58} and nucleic acid^{59,60} systems for purposes other than VSE spectroscopy. For this reason, the interpretation of nitrile absorption shifts in complex samples is of growing interest to theoreticians.^{61–68}

In the work described here, we have introduced the nitrile functional group into the Ras-binding domain (RBD) of Ral guanine nucleotide dissociation stimulator (RalGDS), a downstream effector of Rap1A (Rap). RalGDS can also bind to the human oncoprotein p21^{Ras} (Ras), a structural analog of Rap. Ras is the canonical member of a family of guanosine triphosphate (GTP)-hydrolyzing proteins that switch between an ON state when bound to GTP and an OFF state when bound to guanosine diphosphate (GDP) in the regulation of signal transduction pathways.⁶⁹ In the ON state, Ras binds to a number of downstream effectors for propagation of chemical signals that regulate cell division, cell survival, and apoptosis.^{70–73} Mutations to Ras are found in $\sim 30\%$ of human cancer tumors.⁶⁹ Several of these mutations are known to prevent GTP hydrolysis, thus leaving the protein permanently in the ON state and causing uncontrolled cell growth and cancer. This central role in the formation and growth of human cancers has made Ras a focus of research in molecular oncology. Toward this end, structures of monomeric Ras, its effector proteins, and Ras-effector complexes have been characterized by crystallography and NMR.^{74–78} Although proteins in the Ras family possess a tremendous degree of structural homology, measurement of thermodynamic (ΔG) and kinetic (K_d) parameters indicate high interactive specificity between Ras-like GTPases with their appropriate downstream effectors.^{79–81} For example, Ras and Rap have nearly identical structures and effector binding surfaces and bind to nearly identical downstream effectors (rmsd of 0.7 Å for homologous residues).^{74–77} Despite this, they are not kinetic competitors⁸⁰ and have vastly different binding thermodynamics.^{79,81} Notably, this discriminatory specificity has been observed in vitro, where considerations such as the regulation of gene expression or posttranslational effects on cellular trafficking and location are of no concern. Raf (a downstream effector of Ras) and RalGDS can each bind to the Switch I domain (residues 29–42) of the ON state of both Ras and Rap with a RBD ~ 80 amino acids long that can be expressed and purified independently of the rest of the protein.^{77,82–84} Although the RBD of these two proteins has only 13% sequence homology,⁷⁵ their tertiary structures are almost

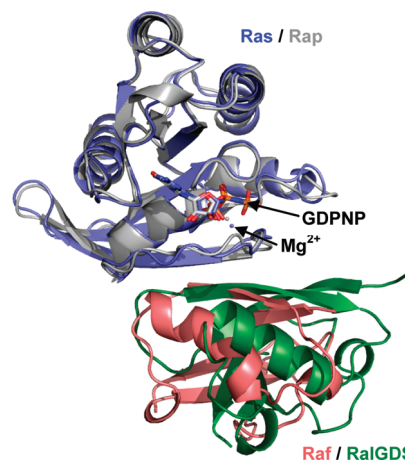


Figure 1. Crystal structure of Ras (with mutation E31K, blue) bound to the Ras binding domain of RalGDS (green, 1LFD)⁷⁵ overlaid with the crystal structure of Rap (with mutation K31E, gray) bound to the Ras binding domain of Raf (salmon, 1GUA).⁷⁶

identical, seen in structures of the protein–protein complexes at resolutions less than 2.1 Å.^{74–77} The remarkable structural similarity of Ras and Rap in the ON state bound to different downstream effectors is shown in Figure 1. These proteins therefore provide an opportunity to explore the contribution of electrostatic fields on interface formation in which structural elements are controlled for as much as possible by the similar structures of the two binding interfaces.

In this report, we describe the systematic investigation of electrostatic fields at the interface of the RBD of RalGDS when bound to either Ras or Rap. Mutations to cysteine were introduced at 11 amino acids on RalGDS that line the interface of the complex with either Ras or Rap. Each cysteine was then chemically modified to thiocyanate, providing systematic incorporation of the nitrile probe molecule throughout the protein–protein interface. Changes in the absorption energy of the thiocyanate probe in each mutant upon complex formation were then related directly to the change of the strength of the local electrostatic field in the immediate vicinity of the probe, thus forming a comprehensive experimentally measured map of electrostatic fields at the Ras–RalGDS and Rap–RalGDS interfaces. These measurements were compared with calculations of the probe’s ensemble-averaged solvent-accessible surface area using structures from molecular dynamics simulations of the thiocyanate-labeled RalGDS mutants in explicit water. We also compared the infrared absorption measurements with calculations of ensemble-averaged electrostatic field at the thiocyanate probe using the Poisson–Boltzmann (PB) equation. This direct comparison of fields measured experimentally and calculated from PB is a preliminary assessment of the accuracy of this simple, commonly used biomolecular electrostatics approach. These results are the first such experimental data of electrostatic fields at a protein–protein interface, and they provide insight into the physical mechanisms of specificity of Ras–effector interactions.

Materials and Methods

A. Protein Expression and Purification. RalGDS and Mutants. The 97-residue Ras binding domain (RBD) of RalGDS was taken from residues 790–886.⁸¹ For clarity, we adopt the numbering convention of a RalGDS crystal structure, 1LFD,⁷⁵ which indexes the glycine at position 797 in RalGDS as G14. The residue index numbers in this manuscript therefore cor-

respond to the protein databank (pdb) file 1LFD. The gene was synthesized and cloned into the pET-15b expression vector (Novagen) by GenScript (Piscataway, NJ), and the sequence was confirmed. Amino acid mutations were made using the Quikchange mutagenesis kit (Stratagene) with PCR primers obtained from Sigma-Aldrich. The mutations C16A and C17A were used to remove both wild type cysteines, generating a protein construct with no cysteine residues that we refer to hereafter as Ral β . Wild type and mutant plasmids were transformed into the *Escherichia coli* strain BL21(DE3) (Novagen) for protein expression. One liter cultures of sterilized TB media with 100 μ g/mL ampicillin were inoculated with the plasmid-containing *E. coli* and agitated for ~4–5 h at 37 °C. Expression of the protein was induced with the addition of 1 mM isopropyl β -D-1-thiogalactopyranoside (IPTG, Sigma). The temperature was reduced to 18 °C, and the culture was agitated for 16 h. The cells were then collected by centrifugation; resuspended in a lysis buffer of 50 mM sodium phosphate pH = 8, 300 mM NaCl, and 10 mM imidazole; flash frozen; and stored at –20 °C until further use.

Cells were thawed and disrupted by sonication. The lysate was centrifuged, and the supernatant was passed through a 10 μ m filter. The clarified lysate was passed through a gravity column containing Ni(II)-nitrilotriacetic acid (Ni-NTA) agarose (Qiagen) two to four times. The column was then washed with 10 column volumes of lysis buffer, followed by elution of the protein with 50 mM sodium phosphate pH = 8, 300 mM NaCl, 500 mM imidazole. The protein was then exchanged into thrombin cleavage buffer (20 mM Tris pH = 8, 150 mM NaCl, 2.5 mM CaCl₂) with a fast protein liquid chromatography (FPLC) Hi-Prep 26/10 desalting column (GE Healthcare) flowing at 10 mL/min, then incubated with thrombin (EMD, approximately 50 units of thrombin per estimated 50 mg of protein) overnight at 4 °C. The cleaved protein was exchanged into loading buffer (50 mM Tris pH = 8) with the desalting column, then loaded onto a 5 mL Fast Flow Q (GE Healthcare) anion exchange column at a rate of 2.4 mL/min. The column was washed with 5 column volumes of loading buffer, then eluted with a gradient of 0–100% elution buffer (50 mM Tris pH = 8, 1 M NaCl) in 12 min. The purified protein was then exchanged into labeling buffer (50 mM Tris pH = 7.5, 100 mM NaCl), flash frozen, and stored at –80 °C. The purity of the final cleaved product was determined by sodium dodecyl sulfate polyacrylamide gel electrophoresis (SDS–PAGE) and electrospray ionization mass spectrometry (ESI-MS). Typical yields were ~100–250 mg of purified protein per liter of growth media.

His-TEV. A plasmid containing a hexa-histidine-tagged tobacco etch virus protease (His-TEV) with the mutation S219V was obtained from Addgene (Addgene plasmid 8827) in *E. coli* strain BL21(DE3)-RIL.⁸⁵ Cultures grown in 1 L of TB were sterilized with 100 μ g/mL ampicillin and 30 μ g/mL chloramphenicol, then agitated for ~4 h, after which protein expression was induced by addition of IPTG to 1 mM. The temperature was reduced to 30 °C, and the cultures were agitated for 4 h. The cells were collected by centrifugation; resuspended in a buffer of 50 mM sodium phosphate pH = 8, 100 mM NaCl, 10% glycerol, 25 mM imidazole; flash frozen; and stored at –20 °C until further use. To purify, the cells were thawed and disrupted through sonication. Polyethylenamine was added to 0.1%, and the lysate was centrifuged to pellet cell debris. The clarified lysate was passed through a 10 μ m filter and loaded onto a 5 mL His-Trap FF column (GE Healthcare) at a rate of 1.2 mL/min. The column was washed until the monitored

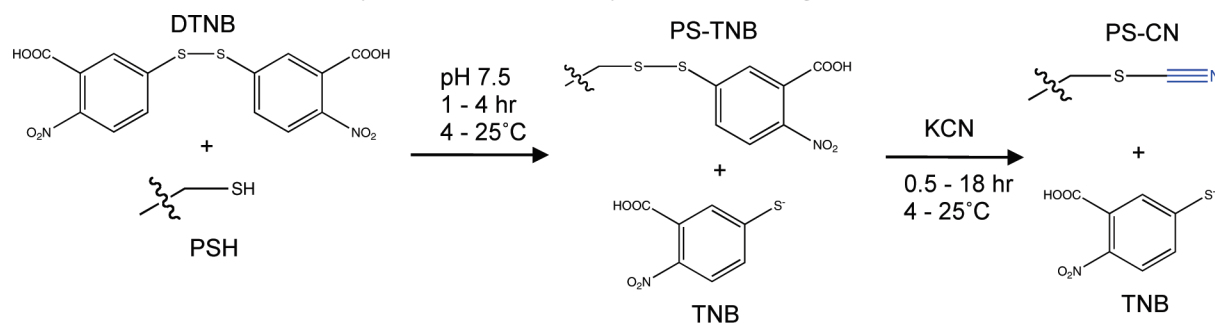
absorbance at 280 nm returned to baseline, then the protein was eluted with a linear gradient of 0–100% 50 mM sodium phosphate pH = 8, 100 mM NaCl, 10% glycerol, 200 mM imidazole at a flow rate of 1.2 mL/min in 20 min. Ethylenediaminetetraacetic acid (EDTA) and dithiothreitol (DTT) were added to the purified protein to a concentration of 1 mM each, and the solution was concentrated by centrifugation then loaded onto an S-100 gel filtration column (GE Healthcare) previously equilibrated in 25 mM sodium phosphate pH = 8, 200 mM NaCl, 10% glycerol, 2 mM EDTA, 10 mM DTT. The protein eluted in 140 mL; this aliquot was flash frozen and stored at –80 °C. Typical yields were 30–60 mg of purified protein per liter of growth media.

WT Ras. The expression vector for WT H-Ras, residues 1–166 was a generous gift from the Kuriyan laboratory.⁸⁶ The gene was expressed in pProEX (Invitrogen) with a hexa-histidine tag that was separated from the protein construct by a cleavage site for His-TEV. The plasmid was transformed into the *E. coli* strain BL21(DE3) for recombinant expression. WT Ras was expressed in 1 L TB cultures according to the procedure described above for RalGDS. The clarified lysate was passed through a 10 μ m filter, loaded onto a 5 mL His-Trap FF column (GE Healthcare) by FPLC at a rate of 2.4 mL/min, then washed with 10 column volumes of lysis buffer or until the monitored absorbance at 280 nm returned to baseline. The protein was then eluted off the column with a gradient of 0–100% elution buffer (50 mM sodium phosphate pH = 8, 300 mM NaCl, 500 mM imidazole) at a flow rate of 1.0 mL/min over 30 min. The protein was then exchanged into His-TEV cleavage buffer (50 mM Tris pH = 8, 50 mM KCl). Approximately 1 mg of His-TEV per 10 mg estimated WT Ras was added and incubated overnight at 4 °C. Potassium chloride (350 mM) and imidazole (20 mM) were then added to the cleaved Ras solution, and the protein was loaded onto a second 5 mL FPLC His-Trap FF column at a rate of 1.2 mL/min. The cleaved WT Ras protein was collected in the flow-through. The column was then washed with 100% elution buffer to elute any uncleaved His-tagged Ras, His-TEV, and the hexa-histidine tag. The protein was then exchanged into labeling buffer with a HiPrep 26/10 desalting column (GE Healthcare).

The protein active site was loaded with guanosine 5'-[β , γ -imido]triphosphate trisodium salt hydrate (GDPNP, Sigma), a nonhydrolyzable GTP analog. The solution was spiked with 5 mM DTT, 4 mM EDTA, and a 3-fold excess of GDPNP and incubated at 4 °C for 2–3 h. Ten millimolar MgCl₂ was then added and allowed to incubate for an additional 30 min at 4 °C. The solution was then concentrated to <3 mL and loaded onto a Superdex 75 10/300 GL gel filtration column (GE Healthcare) equilibrated in labeling buffer. WT Ras bound to GDPNP eluted in 11–15 mL, and the purity of the final product was determined by SDS–PAGE and ESI-MS. The protein was then flash-frozen and stored at –80 °C until further use. Typical yields were ~20–40 mg of purified protein per liter of growth media.

WT Rap. The WT Rap construct was composed of residues 1–167 of Rap1A. The gene was synthesized and cloned into the pET-15b expression vector (Novagen) by GenScript (Piscataway, NJ), and the sequence was confirmed. This vector was transformed into the *E. coli* strain Arctic Express (DE) (Stratagene) for expression. One liter cultures of TB containing no antibiotics were inoculated with WT Rap and agitated for ~4–6 h at 37 °C. The temperature was reduced to 11 °C, and protein expression was induced by the addition of 100 μ g/mL ampicillin, 100 μ g/mL gentamycin (Sigma), 1 mM IPTG, and 1 mM DTT.

SCHEME 1: Introduction of a Thiocyanate Probe onto a Cysteine-Containing Protein, PSH



The solution was then agitated for 24 h. The cells were pelleted by centrifugation, resuspended in lysis buffer containing 1 mM DTT and 10% glycerol, flash frozen, and stored at -20°C until further use.

WT Rap was isolated from the lysate through hexa-histidine affinity with Ni-NTA by the procedure described for WT Ras, with the modification that 1 mM DTT and 10% glycerol were added to all buffers. The His-tagged protein was eluted in buffer containing 1 mM DTT and 10% glycerol. This was exchanged into thrombin cleavage buffer, thrombin was added to a concentration of ~ 100 U of thrombin per 50 mg estimated protein, and incubated at 4°C overnight. The cleaved protein was further purified by anion exchange chromatography and exchanged into labeling buffer as described above for RalGDS and mutants.

GDPNP was loaded into the WT Rap active site by adding 10% glycerol, 5 mM DTT, 4 mM EDTA, and 3-fold excess of GDPNP and incubated at 4°C for 2 h. Magnesium chloride was then added to 10 mM and allowed to incubate for an additional 30 min. The solution was then concentrated to <5 mM and loaded onto a HiLoad 16/60 Superdex 200 gel filtration column (GE Healthcare) previously equilibrated in labeling buffer at a rate of 1.0 mL/min and eluted between 95 and 100 mL. Purity of the final product was determined by SDS-PAGE and ESI-MS. The protein was then flash-frozen and stored at -80°C until further use. Typical yields were ~ 5 – 10 mg of purified WT Rap per 1 L of growth media.

B. Introduction of the Nitrile Functional Group. The conversion of a cysteine thiol into the thiocyanate Stark probe was achieved by the reaction shown in Scheme 1, which has been described previously.⁴⁸ Two molar equivalents of 5,5'-dithiobis(2-nitrobenzoic acid) (DTNB, Sigma-Aldrich) were added to a Ral β mutant containing one solvent-exposed cysteine residue (PSH) and incubated at room temperature for 2–14 h, forming the protein-bound thionitrobenzoic acid disulfide (PS-TNB). The extent of the reaction was monitored by observing the formation of the TNB⁻ side product by its absorption at 412 nm ($\epsilon_{412} = 13\,600\text{ M}^{-1}\text{ cm}^{-1}$). After 1 equiv of TNB⁻ had been generated, 100 equiv of potassium cyanide (KCN) was added to displace the protein-bound TNB and generate the protein–thiocyanate complex PS-CN. The extent of reaction was again observed by absorption of the TNB⁻ side product at 412 nm. At the end of the reaction, a PD-10 desalting column (GE Healthcare) was used to remove excess TNB⁻ and CN⁻ and return the labeled protein to labeling buffer. In most cases, ESI-MS was used to confirm the addition of 26 Da to the mass of the purified protein, indicating the presence of the SCN label. The SCN-labeled Ral β mutants are denoted with the subscript “SCN.”

Two Ral β mutants, M30C and K52C, did not react with DTNB under these conditions, but had to be denatured in 8 M

urea to expose the reactive cysteine residue. After exchanging into a solution of 8 M urea, 50 mM Tris pH = 8, 100 mM NaCl with a PD-10 desalting column, these two mutants were exposed to DTNB and KCN as described above. After the labeling reaction was complete, a PD-10 desalting column was again used to exchange the protein back into labeling buffer. This resulted in the simultaneous refolding of the protein, which was confirmed for Ral β M30C_{SCN} by gel filtration chromatography (Superdex 200, GE Healthcare).

C. Kinetic Analysis of SCN-Labeled Ral β Mutants Docking to WT Ras and WT Rap. The docked complex of either WT Ras or WT Rap with the SCN-labeled Ral β mutant was formed by incubating Ral β -SCN with 2 equiv of the desired binding partner (Ras or Rap) at 4°C for up to 16 h. Gel filtration chromatography (Superdex 200 equilibrated in labeling buffer) was used to confirm the formation of the docked WT Ras-Ral β G28C_{SCN} complex at ~ 30 kDa. The dissociation constant, K_d , of the interaction was measured using a guanine nucleotide dissociation inhibition (GDI) assay described before.⁸⁰ WT Ras (100 nM) or WT Rap bound to the fluorescently labeled GTP 2'-(or 3')-O-(*N*-methylantraniloyl)guanosine 5'-triphosphate trisodium salt (mant-GTP, Invitrogen) were incubated with varying concentrations of the RBD of interest (WT RalGDS or a SCN-labeled Ral β mutant) at 37°C for 1–2 h in a 96-well unskirted PCR plate (BioRad). The dissociation of mant-GTP was initiated by the addition of 250 mM GDPNP, and the plate was quickly covered then centrifuged for 30 s to mix the reaction. Decay in the fluorescence of mant-GTP was monitored in a real-time qPCR system (Stratagene, MX3005P) set with excitation and emission wavelengths of 365 and 450 nm, respectively. The initial rate of this decay was taken to be the observed rate of the dissociation reaction, k_{obs} . This was fit to eq 1 to determine K_d :

$$k_{\text{obs}} = k_{-1} - k_{-1}^* \frac{R_0 + E_0 + K_d - \sqrt{(R_0 + E_0 + K_d)^2 - 4R_0E_0}}{2R_0} \quad (1)$$

where R_0 is the concentration of WT Ras or WT Rap, E_0 is the concentration of the RBD, and k_{-1} is the rate constant for mant-GTP dissociation from Ras in the absence of the RBD.⁸⁰

D. Molecular Dynamics and Continuum Electrostatics Calculations. No pdb structure exists with coordinates for all atoms in our sequence, requiring us to construct a model of Ral β based on the pdb structure 2RGF.⁷⁴ To make the Ral β structure, all side chain atoms except the β carbons were deleted from the two cysteine residues, which were then renamed to ALA. The C-terminal residues RTFT were taken from the pdb structure 1RAX (deposited in the PDB but unpublished) which

ends in KKRTFT, and pasted onto the 2RGF structure, which ends in KKRT, by aligning the backbone atoms of the common KKRT residues using STAMP⁸⁷ structural alignment in VMD.⁸⁸ The first residues in the 2RGF structure are ALA and LEU; these were changed to SER and HIS by renaming the residues in the pdb file, deleting hydrogen atoms, and renaming, using CD1 of LEU as ND1 of HIS. The N-terminal glycine (GLY 4) was modeled using Avogadro, completing the sequence.⁸⁹ Missing heavy atoms of SER 5 and HIS 6 were added by loading the resulting file into the Amber utility tleap.⁹⁰ The structure was protonated using the GROMACS⁹¹ utility pdb2gmx, using the ffamber03 GROMACS port⁹² of the Amber 2003 force field.⁹³ Throughout all energy minimization, molecular dynamics, and Poisson–Boltzmann calculations, we assumed neutral histidine residues with hydrogens on NE, positively charged lysine and arginine, and negatively charged glutamate and aspartate. The model was then energy-minimized using 50 steps of the steepest descents method, explicitly calculating all van der Waals interactions and all Coulomb interactions in vacuum with dielectric constant 78. After this minimization step, the potential energy was $-1329 \text{ kJ mol}^{-1}$ and the maximum force on any atom was $6498 \text{ kJ mol}^{-1} \text{ nm}^{-1}$ on the backbone C atom of Arg-100 (i.e., a native pdb atom, not one of our modeled atoms).

To generate cyanylated Ral β , residues were renamed to MET in the pdb file (because methionine contains the same number of heavy atoms as cyanocysteine), retaining and renaming any atoms common to the native residue and methionine. In particular: for I18, CG2 was deleted, and CD was renamed to SD; for R20, CZ was deleted; for N27, N29, and N54, OD1 was renamed to SD and ND1 was deleted; for Y31, CD1 was renamed SD, CE1 was renamed CE, and CD2, CE2, CZ, and OH were deleted; and for K52, CD was renamed SD and NZ was deleted. Missing methionine atoms were added using tleap. To complete the mutation to cyanocysteine, the MET atoms CG, SD, and CE were renamed SG, CD, and NE.

Cyanocysteine parameters, other than partial charges, were transferred from the Amber 2003 force field to ffamber03. Only two new atom types, NY and CY, one for each of the nitrile atoms, had to be ported to ffamber03. Partial charges were assigned by generating an *N*-acetyl-*C*-amidocyanocysteine fragment from the G28M backbone using the backbone N of ASN 27 as 3HA, ASN 27 CB as 2HA, ASN 29 CB as 2HA, and backbone TYR 29 C as 3HA and stretching the bonds to these atoms to be equal to that for CA-HA of residue 28. The methionine atoms of residue 28 were renamed to cyanocysteine atoms and their geometry was modified in accordance with calculations of Kharitonov⁹⁴ by moving SG and CD parallel to the CB-SG bond until the CB-SG bond was 1.820 Å, moving CD parallel to the (new) SG-CD bond until the SG-CD bond was 1.684 Å, and placing NE 1.156 Å from CD on the SG-CD axis. Avogadro was used to set the backbone torsions to 180°, to optimize the geometry using default settings, and to modify the CB-SD torsion to 120° (away from the backbone). The CA-CB torsion was then rotated by 30° increments, generating 12 structures, which were used for point-geometry RHF/6-31g* calculations using GAMESS^{95,96} with the electrostatic potential of the electron density recorded at the Connolly surface. Partial charges shown in Table 1 were derived using RESP^{90,97} on the resulting 12 electrostatic potentials and the 12 conformations using default parameters. The magnitudes of these charges were similar to previous calculations on methylthiocyanate.⁶⁵ These charges were used for all subsequent energy minimization, equilibration, and molecular dynamics sampling.

TABLE 1: Cyanocysteine Atom Types and Charges in Units of e^a

| atom | ffamber03 atom type | charge |
|------|---------------------|------------|
| N | amber99_34 | −0.406 610 |
| H | amber99_17 | 0.267 120 |
| CA | amber99_11 | −0.008 715 |
| HA | amber99_19 | 0.114 760 |
| CB | amber99_11 | −0.104 961 |
| HB1 | amber99_19 | 0.111 325 |
| HB2 | amber99_19 | 0.111 325 |
| SG | amber99_47 | −0.094 239 |
| CD | amber03_CY | 0.364 643 |
| NE | amber03_NY | −0.438 622 |
| C | amber99_2 | 0.606 088 |
| O | amber99_41 | −0.522 115 |

^a The nitrile bond is composed of atoms CD and NE, which are represented by the new ffamber03 atom types ffamber03 CY and ffamber NY. Other atom types are from ffamber03, which are named with the stem “amber99” in the ffamber03 force fields.

The 11 cyanocysteine-containing models were then subjected to 100 steps of steepest-descents energy minimization using GROMACS version 4.0.5. All van der Waals and Coulomb interactions (using a vacuum dielectric of 78) were calculated. Otherwise, all settings were the GROMACS defaults. This was done primarily to straighten the thiocyanate group from the methionine conformation.

The thiocyanate CB-SG torsion was rotated by 45° increments in each of the 11 mutants, yielding eight rotated structures, including the 0° cis conformation. These structures were then subjected to a second round of vacuum energy minimization using GROMACS dihedral restraint potentials centered at 0, 45, 90, 135, 180, 225, 270, and 315°, flat within 45° of the center, and harmonic with force constant of $1000 \text{ kJ mol}^{-1} \text{ rad}^{-2}$ outside of that range. All van der Waals and Coulomb interactions (vacuum dielectric 78) were calculated; otherwise, the simulation settings were GROMACS defaults. In addition, another 100 steps of vacuum energy minimization were run for each mutant without the thiocyanate torsion being restrained using the initial coordinates output from the first energy minimization step. This procedure yielded nine starting structures for each mutant. The restraint potential described was applied to all the subsequent minimization and sampling steps; equilibration was performed with all solute atoms restrained, as described below.

The nine energy-minimized structures for each of the 11 mutants were then placed in dodecahedral simulation boxes using the GROMACS tool editconf, specifying that the solute should be no less than 1.2 nm from the edge of the box. Tip3p water molecules⁹⁸ were added to each of the 99 systems. Sodium ions (five for R20C, K32C, and K52C and four for all others) were added using the GROMACS tool genion with tpr files compiled using the energy minimization parameters (ie, no periodic boundary conditions and all Coulombic interactions calculated with a dielectric constant of 78). Otherwise, default settings were used. After solvation, the models were subjected to a final steepest-descents energy minimization until either the largest force on any atom was less than $800 \text{ kJ mol}^{-1} \text{ nm}^{-1}$ or 5000 steps, whichever came first. Periodic boundary conditions were employed. van der Waals forces were calculated using a smooth switching function (GROMACS mdp setting “vdw-type=switch”) from 0.7 nm tapering to 0 at 0.8 nm. Coulombic interactions were treated with PME^{99,100} using a real-space cutoff of 0.9 nm, a spacing of 0.12 nm, and interpolation order 4. Otherwise, GROMACS defaults were used.

The solvent was equilibrated for 10 000 2 fs steps, while restraining solute atoms in harmonic potentials with force constants of 1000 kJ mol⁻¹ nm⁻² in each Cartesian direction. Neighbor lists up to a distance of 0.9 nm were updated using a grid-based approach every 10 steps. The PME was used for Coulomb interactions and a switch was used for van der Waals interactions, as in the final energy minimization. The system temperature was maintained at 300 K by using the Langevin integrator with an inverse friction constant of 0.011 ps (close to that of liquid water at 300 K). Bonds to hydrogen were constrained using the SHAKE¹⁰¹ algorithm for the solute and SETTLE¹⁰² for the solvent.

To generate samples, we ran stochastic dynamics simulations on the Stampede cluster at the Texas Advanced Computing Center. These runs were 500 000 2 fs time steps and required ~24 h of computation time. Dihedral restraints were employed, identical to those used in the minimization step, above. The probe orientational free energy was estimated from these umbrella sampling simulations using the weighted histogram analysis method (WHAM).^{103,104} The resulting free energy surface was determined in 5 bins from -180 to 180° and was fit to eq 2:

$$A(\phi) = k + \sum_{n=1}^4 \sin(n\omega(\phi - \phi_0)) \quad (2)$$

where A is the Helmholtz free energy of the torsion centered at ϕ ; and k , ω , and ϕ_0 are the fitting constants. For each mutant, additional 3 ns simulations, hereafter referred to as the “second-stage simulations,” were run using each of the three minima of eq 2 as centers for the dihedral restraint potential. This resulted in 12 simulations for each mutant: 1 unrestrained for 1 ns, 8 restrained at 45° increments from 0 to 315° for 1 ns, and 3 restrained at the fitted free energy minima for 3 ns, totaling 18 ns per mutant. All 18 ns of simulation was used to construct final free energy surfaces using WHAM, but only the second-stage simulations were used for solvent-accessible surface area and electric field calculations.

The solvent-accessible surface area (SASA) of the cyanocysteine residue was calculated using the GROMACS utility `g_sas` using default parameters and a waterlike probe radius of 1.4 Å. SASA was calculated for the whole protein but recorded only for the 12 thiocyanate atoms. The SASA calculation for each snapshot was Boltzmann-weighted at 300 K using the torsional distribution from WHAM. Multiple counts in each bin were averaged together to get a SASA value for that bin before being averaged using the Boltzmann distribution.

The Adaptive Poisson–Boltzmann Solver (APBS)¹⁰⁵ was used to obtain electrostatic potentials from the linearized Poisson–Boltzmann (PB) equation. The software was used to generate automatically configured sequential focusing multigrid calculations consisting of 2 steps with 193 grid points in each dimension. The coarse grid calculation had dimensions of 74 Å in the x and y dimensions and 79 Å in z , centered on the Ralβ molecule. The fine grid calculation had dimensions of 63, 64, and 60 Å in x , y , and z , respectively, again centered on the protein. A multiple Debye–Hückel boundary condition was applied. The calculations included the effects of 150 mM each of positive (+1) and negative (-1) ions with a radius of 2.0 Å. The temperature was 300 K. The molecular surface and ion accessibility coefficients were constructed from a seventh-order polynomial spline using a 0.3 Å support. A trilinear interpolation was used to map charges to nearest-neighbor grid points. The

force constant for the nitrile bond is large, 848 930.0 kJ mol⁻¹ nm⁻² (compared with, for example, 392 459.2 kJ mol⁻¹ nm⁻² for C–C bonds in ffambr03), and therefore, the length of the nitrile bond does not change significantly during simulations. Therefore, the contribution of these charges to the field is expected to be approximately constant throughout the simulation, and for this reason, the charge on these two atoms was taken to be zero for the PB solution. All other charges, as well as atomic radii, were taken from the Amber 2003 force field.

Relative dielectric constants of 2.0 and 78.0 were used for the protein and solvent, respectively. Much higher dielectric constants are commonly used for the solute to obtain Poisson–Boltzmann solutions in problems of this type,²⁷ since point charge force fields do not explicitly model electronic polarizability or structural fluctuations. In the present case, however, we directly included the effects of protein motion by calculating the electrostatic potentials for a large subset of our snapshots from molecular dynamics simulations and averaging the results according to the results from WHAM. In principle, this justifies using a lower dielectric constant. However, because we cannot model polarizability, we use a modest dielectric constant of 2.

The results of the PB calculation were used to construct an electric potential curve of 100 points from the carbon of the nitrile to the nitrogen. The potential near the center of the nitrile bond was invariably linear, so the electric field was calculated to be the negative of the slope at the 50th point of the electrical potential. The field at the bond midpoint was calculated for all second-stage simulation snapshots and averaged in the same manner as with SASA. In addition to PB, we tried a naïve Coulombic calculation in which the field at the bond midpoint was calculated from the electric field due to ffambr03 point charges.

E. Vibrational Spectroscopy. Infrared spectra of the SCN-labeled Ralβ monomers and SCN-labeled Ralβ mutants bound to Ras or Rap were taken in labeling buffer (50 mM Tris pH = 7.5, 100 mM NaCl). Thiocyanate-labeled Ralβ mutants were concentrated by centrifugation to ~2 mM, and vibrational absorption spectra of the monomeric construct were collected at room temperature in a sample cell composed of 2 sapphire windows separated by 125-μm-thick PETE spacers in a Bruker Vertex 70 FTIR. The sample cell was illuminated with light in the range of 2000–2500 cm⁻¹ selected by a broad bandpass filter (Spectrogon, Parsippany, NJ) placed in front of the instrument’s IR source. Spectra were composed of 250 scans collected with a liquid-nitrogen-cooled indium antimonide (InSb) detector at 0.5 cm⁻¹ resolution. Uncertainty in absorption energy is reported as the standard deviation of at least four measurements.

To form the docked Ras-RBD or Rap-RBD complex, the SCN-labeled Ralβ mutants were incubated with 2 mol equiv of either WT Ras or WT Rap at 4 °C overnight. The solution was then concentrated by centrifugation to ~2 mM. The vibrational absorption energy of the thiocyanate group in the docked complex was then measured in the sample cell described above. The observed change in absorption energy of the thiocyanate, $\Delta\nu_{\text{obs}}$, was then related to the change in the electrostatic environment in the vicinity of the probe caused by the protein–protein interaction, $\Delta\bar{F}_{\text{dock}}$, through eq 3,

$$\Delta E = hc\Delta\nu_{\text{obs}} = -\Delta\vec{\mu}_{\text{SCN}} \cdot \Delta\vec{F}_{\text{dock}} \quad (3)$$

where $\Delta\vec{\mu}_{\text{SCN}}$, also called the Stark tuning rate, has been previously measured as 0.7 cm⁻¹/(MV/cm).⁴⁸ This dipole vector is taken to point from the nitrogen atom to the carbon atom of

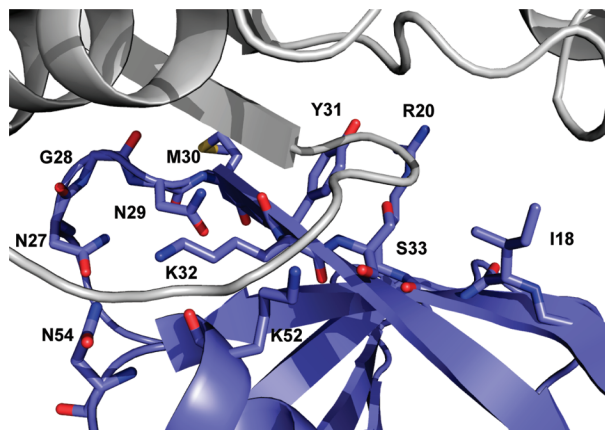


Figure 2. Crystal structure of the docked Ras (gray)–RalGDS (blue) complex, highlighting amino acids from RalGDS that participate in the stable protein–protein interaction and that were selected for positioning the thiocyanate VSE probe in this study. Structure prepared from 1LFD.⁷⁵

the thiocyanate.⁶¹ Thus, a 1 MV/cm increase in electrostatic field upon docking will shift the absorption energy of the thiocyanate probe by -0.7 cm^{-1} .

Results and Discussion

A. Simulations of the Thiocyanate Functional Group on Ral β . The formation of any noncovalent protein–protein interface is the result of a subtle interplay between structural effects based on molecular shape and electrostatic effects caused by solvation, residue identity, interfacial surface area, the presence of structural waters, and charge balance. The binding interfaces of the GTPases Ras and Rap are structurally quite similar, yet are able to distinguish a functionally appropriate downstream effector (i.e., Raf versus RalGDS) for binding. On the basis of a 2.1 Å resolution crystal structure of Ras E31K docked with the RBD of RalGDS,⁷⁵ 11 residues on the surface of RalGDS that participate in the docked Ras–RalGDS complex were selected as positions for systematic incorporation of the nitrile VSE probe. These residues are identified in Figure 2. These 11 amino acids are all exposed to buffer at the surface of the Ral β monomer, then become immersed in the dense interfacial structure formed when the two proteins dock. They are directly exposed to electrostatic fields created at the protein–protein interface, and including our VSE spectroscopic probe on these amino acids interrogates the protein–protein interface systematically. These residues are diverse in chemical identity, displaying hydrophobic (I18, G28, M30), polar (N27, N29, Y31, S33, N54), and charged (R20, K32, K52) functional groups, all of which contribute to the free energy of the formation of the stable Ras–RalGDS interface through electrostatic interaction mechanisms. Furthermore, the crystal structure shows that five of these residues (R20, Y31, K32, K52, and N54) participate in hydrogen bonding interactions either with the Switch I domain of Ras E31K or with crystallographically resolved water molecules buried at the protein–protein interface.⁷⁵ The residues that comprise the RalGDS side of the protein–protein interface are diverse in chemical identity and electrostatic potential and represent a comprehensive snapshot for initial experiments on the electrostatic contributions to the formation of a protein–protein interface.

Because the Stark effect is caused by the interaction of two vectors ($\Delta\vec{\mu}_{\text{SCN}}$ and $\Delta\vec{F}_{\text{dock}}$), interpretation of the strength and direction of an electrostatic field from the experimental data of thiocyanate probe absorption energies requires a reasonably

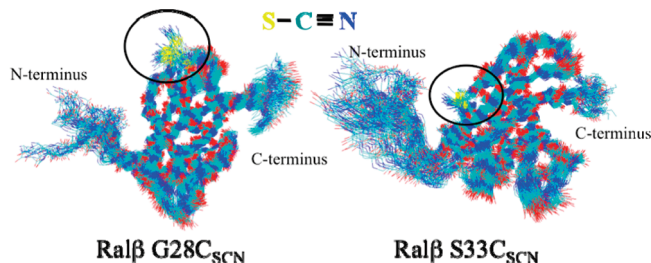


Figure 3. Structures from simulation of two Ral β mutants, G28C_{SCN} (left) and S33C_{SCN} (right), at a 50 ps time resolution. Only backbone atoms and cyanocysteine atoms (circled) are shown. The structures were aligned by a least-squares fit to the protein structures generated by equilibration using the backbone atoms of residues 15–100. Snapshots are from three different trajectories with torsional restraint potentials of approximately -60 , 60 , and 120° ; that is, these are not Boltzmann-weighted images. The nitrile on G28C_{SCN} shows a much greater range of motion than it does on S33C_{SCN}.

accurate understanding of the location of the probe in the protein system. In the absence of crystal structures of the SCN-labeled Ral β mutants, we performed molecular dynamics simulations to generate the thiocyanate probe's torsional free energy surface and assemble an ensemble of reasonable structures for analysis. Backbone atoms and the cyanocysteine side chain from simulations of two representative SCN-labeled Ral β mutants, G28C_{SCN} and S33C_{SCN}, are shown in Figure 3. These snapshots are taken from the 3 ns second-stage simulations that were performed with the probe torsion restrained at the alkane dihedral angles of 60 , 180 (trans) and 300° at a temporal resolution of 50 ps. Although these are not Boltzmann-weighted structures, the tight distribution of the peptide backbone atoms demonstrates that the protein fold is stable. These structures also illustrate the range of different motion available to the thiocyanate at different locations; unsurprisingly, when the probe is on a loop, as in G28C_{SCN}, the nitrile appears to be more mobile, and when it is on a strand, as in S33C_{SCN}, it appears to be less mobile.

The probe orientational distribution for each mutant is shown in Figure 4. In eight mutants, the probe favors the simple alkane orientations of -60 , 60 , and 180° , with a tendency to prefer trans ($\phi = 180^\circ$). Three mutants deviate from this pattern. K32C_{SCN} appears to favor all three alkane orientations but the density near trans is suppressed and more structured than in the other mutants. In N29C_{SCN} the trans density is almost completely suppressed. In K52C_{SCN}, the torsional angle at -60° is preferred to other observed torsions. Interestingly, two of these mutants, K32C_{SCN} and K52C_{SCN} are ill-behaved in our correlations of SASA to measured thiocyanate absorption energy, as discussed below.

B. Vibrational Spectroscopy of SCN-Labeled Ral β Monomers. Vibrational absorption spectra of the SCN probe molecule were collected on SCN-labeled Ral β mutants in labeling buffer, then again after incubating this protein with WT Ras or WT Rap. Representative examples of these absorption spectra are shown in Figure 5. The vibrational frequency of Ral β G28C_{SCN} in labeling buffer was determined to be $2159.8 \pm 0.1 \text{ cm}^{-1}$. Because the protein–protein interface involves approximately a dozen amino acids contributed from both proteins, the complete experiment encompasses the data accumulated from moving the thiocyanate probe systematically throughout the interface, which in this case requires moving the probe along the Ral β protein surface. These results are summarized in Figure 6 and tabulated in Table 2. Figure 6 shows the thiocyanate absorption energy for each of the 11 labeled Ral β mutants. There appear to be three distinct electrostatic environments experienced

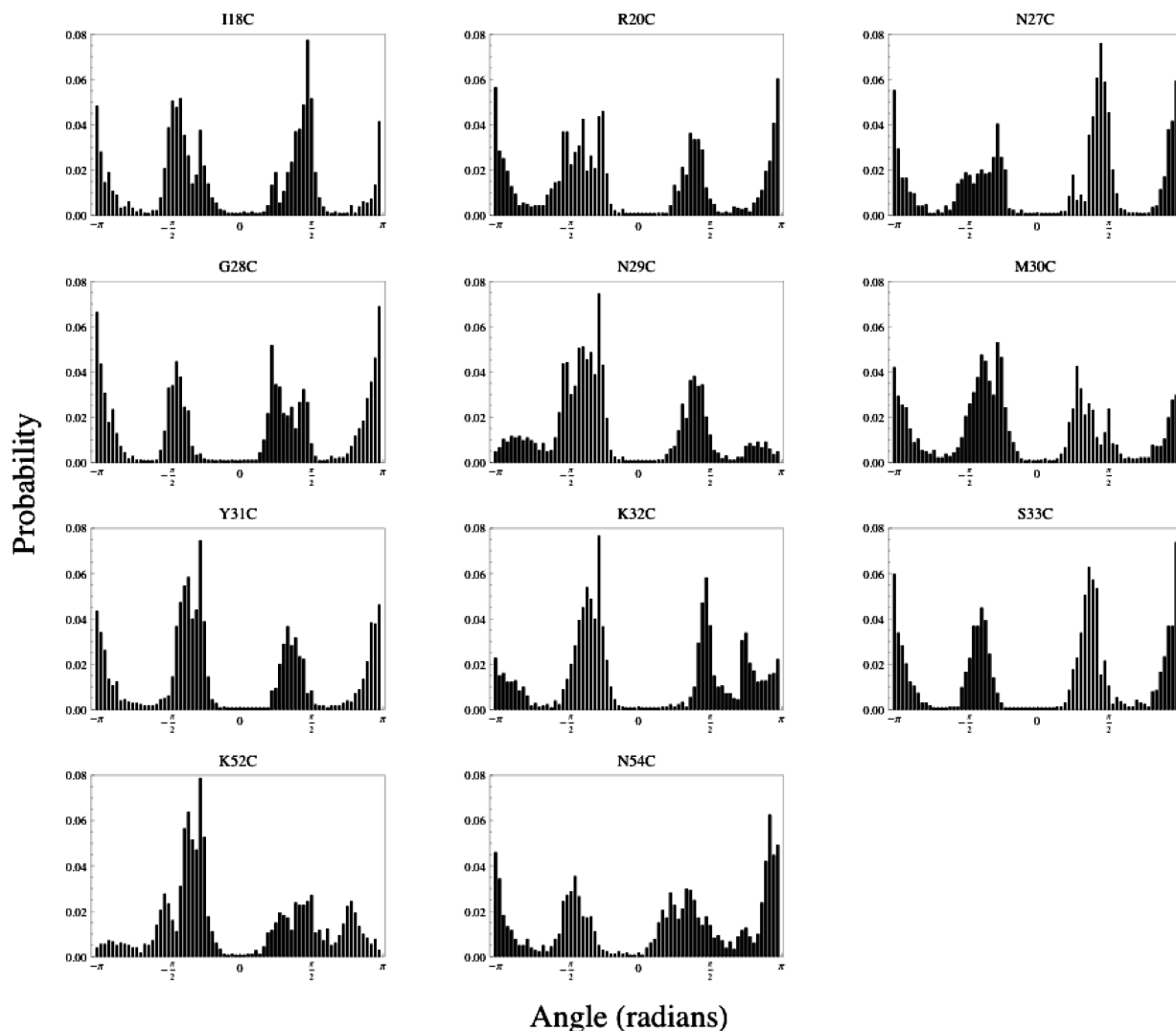


Figure 4. Torsional angle distributions of the thiocyanate probe on the 11 SCN-labeled Ral β mutants as derived from WHAM. Eight mutants have three probability maxima separated by $\sim 120^\circ$, as expected for alkanes. Three mutants, N29C_{SCN}, K32C_{SCN}, and K52C_{SCN}, have more complicated distributions with at least one of these three preferred alkane orientations suppressed.

by the nitrile probe based on its location on the Ral surface. Differences in the absorption energy of the nitrile vibrational probe on SCN-labeled Ral β mutants could reflect the extent of the nitrile's exposure to the protein surface, to water molecules, and to participation in hydrogen bonding interactions,⁶⁵ since all data were collected under the same solvent conditions (labeling buffer).

Several observations indicate that cyanocysteine residues that were more exposed to solvent are correlated with lower thiocyanate absorption energies. First, we computed the Boltzmann-weighted solvent-exposed surface area of the cyanocysteine residue in each Ral β mutant from our molecular dynamics sampling. The relationship between SASA and measured absorption energy is shown in Figure 7. There appears to be a slight negative correlation between the calculated SASA determined from a Boltzmann-weighted ensemble of structures and measured vibrational energy. The correlation is weak, with $r^2 = 0.296$, but cyanocysteines at positions K32C_{SCN} and K52C_{SCN} appear to be outliers in this analysis. Fitting this correlation without the wild-type charged residues (R20C_{SCN}, K32C_{SCN}, and K52C_{SCN}) yielded a stronger correlation ($r^2 = 0.647$). This fitting does not propose a mathematical relationship between SASA and measured absorption energy, but merely highlights the observation that experimentally measured thiocyanate absorption

energies are subtly correlated with exposure to water at the protein–water interface.

Second, we measured the effect of the solvent pH on the absorption energy of several SCN-labeled Ral β mutants of differing calculated SASA. Cyanocysteine residues that are more exposed to the solvent should show a larger difference to a change in solvent pH. To this end, G28C_{SCN}, S33C_{SCN}, and R20C_{SCN} were exchanged into a buffer of higher pH (50 mM Tris pH = 9.2, 100 mM NaCl), and the thiocyanate absorption energy was measured. R20C_{SCN}, with a low calculated SASA, had no change in its absorption energy, but the mutant with the highest calculated SASA, G28C_{SCN}, showed an increase in frequency of 1.8 cm^{-1} compared with the measured value at pH = 7.5. Finally, we observed that S33C_{SCN} was intermediate between these two extremes, with a change in thiocyanate frequency of $+0.3\text{ cm}^{-1}$. These data support the prediction from the calculated SASA that these three residues rank in order of solvent exposure with G28C_{SCN} > S33C_{SCN} > R20C_{SCN}.

Third and finally, as explained below, the residues G28C_{SCN} and K32C_{SCN} demonstrated large shifts to higher absorption energies upon formation of the docked protein–protein complex, which will most likely result in *less* solvent exposure for every residue. Taken together, these three observations are consistent with the hypothesis that higher energy absorptions occur at probe

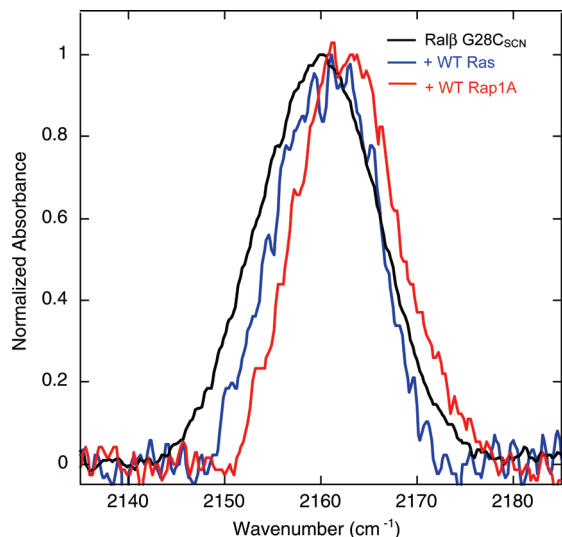


Figure 5. Normalized absorbance of thiocyanate on Ral β G28C_{SCN} measured in labeling buffer (black, $\bar{\nu}_{\text{obs}} = 2159.8 \pm 0.1$), then in the presence of a slight molar excess of WT Ras (blue, $\bar{\nu}_{\text{obs}} = 2161.6 \pm 0.2$) or WT Rap (red, $\bar{\nu}_{\text{obs}} = 2162.0 \pm 0.2$).

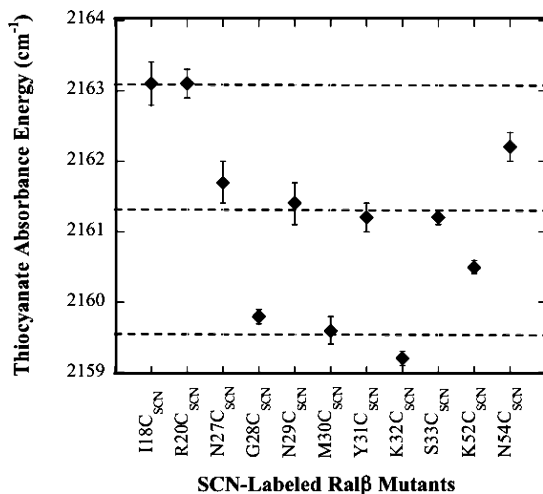


Figure 6. Absorption energy of the nitrile probe on 11 SCN-labeled mutants of Ral β (indicated on the x -axis). Data were collected in solutions of 2 mM SCN-labeled Ral β mutant in labeling buffer at room temperature. Error bars represent 1 standard deviation of multiple experiments, and dashed lines are added to guide the eye.

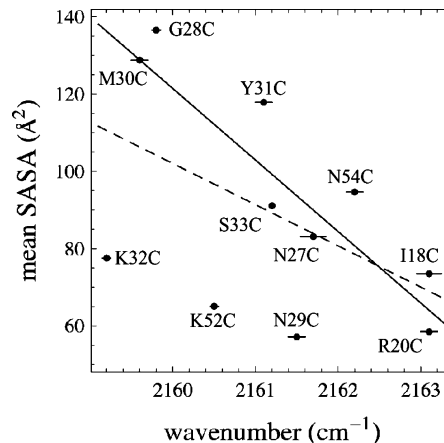


Figure 7. Boltzmann-weighted SASA from simulations versus measured absorption energy for the SCN-labeled Ral β mutants. Horizontal lines reflect the experimental uncertainty shown in Figure 6. SASA was calculated using a probe the size of a water molecule (1.4 Å) on the entire protein molecule; the portion of the SASA associated with cyanocysteine atoms is plotted. A linear fit to all data points (dotted line) has $r^2 = 0.296$ and a root-mean-square deviation from the data of 22 Å^2 . Fitting all mutants except those charged in Ral β (R20C_{SCN}, K32C_{SCN}, K52C_{SCN}, solid line) gives a fit with $r^2 = 0.647$ and a root-mean-square deviation of 15 Å^2 .

locations that are dominated by interactions with the protein, and lower energy absorptions are due to more exposure to the solvent. According to this hypothesis, the nitriles at positions G28C_{SCN}, M30C_{SCN}, and K32C_{SCN} are interacting with more water than protein in the monomeric state, whereas all of the other residues are interacting predominantly with the surface of the Ral β protein. Upon binding, G28C_{SCN} and K32C_{SCN} become buried, and as a result, their energies increase (binding data on M30C_{SCN} is not available, as described below).

However, this interpretation contradicts both experimental and theoretical work from other laboratories. Nitriles have previously been used to probe the extent of hydration of a particular amino acid within a folded protein, with higher energy absorptions indicating the nitrile is exposed to water and lower energy absorptions indicating the nitrile is in a more hydrophobic location caused by three-dimensional biomolecular structure and sequestration from water.^{53,106} Subsequent calculations of the nitrile absorption energy in water versus aprotic solvents seem to support this interpretation.^{62,65} To establish a scale for this effect, we measured the absorption energy of methyl thiocyanate (MeSCN) in labeling buffer ($2162.6 \pm 0.1 \text{ cm}^{-1}$), which should characterize a completely solvent-exposed thiocyanate. Because

TABLE 2: Measured SCN Vibrational Frequencies ($\bar{\nu}_{\text{obs}}$) and Full Width at Half Maximum (fwhm) of SCN-Labeled Ral β Mutants in Labeling Buffer; the Observed Changes to These Quantities ($\Delta\bar{\nu}_{\text{obs}}$ and $\Delta(\text{fwhm})$) upon Docking Each Mutant to WT Ras and WT Rap; $\Delta\vec{F}_{\text{dock}}$ obtained from eq 3

| Ral β mutation | $\bar{\nu}_{\text{obs}}$ (cm $^{-1}$) ^a | fwhm (cm $^{-1}$) ^a | WT Ras | | | WT Rap | | |
|----------------------|---|---------------------------------|--|---------------------------------------|-------------------------------------|--|---------------------------------------|-------------------------------------|
| | | | $\Delta\bar{\nu}_{\text{obs}}$ (cm $^{-1}$) | $\Delta\vec{F}_{\text{dock}}$ (MV/cm) | $\Delta(\text{fwhm})$ (cm $^{-1}$) | $\Delta\bar{\nu}_{\text{obs}}$ (cm $^{-1}$) | $\Delta\vec{F}_{\text{dock}}$ (MV/cm) | $\Delta(\text{fwhm})$ (cm $^{-1}$) |
| I18C _{SCN} | 2163.1 (0.3) | 12.1 (0.5) | −0.8 | 1.1 | 0.3 | −0.9 | 1.3 | −2.1 |
| R20C _{SCN} | 2163.1 (0.2) | 12.5 (0.9) | −0.9 | 1.3 | −2.3 | −1.5 | 2.1 | −2.1 |
| N27C _{SCN} | 2161.7 (0.3) | 12.0 (0.8) | 1.8 | −2.6 | −0.9 | 0.8 | −1.1 | −0.5 |
| G28C _{SCN} | 2159.8 (0.1) | 13.8 (0.6) | 1.8 | −2.6 | −2.5 | 2.2 | −3.1 | −2.3 |
| N29C _{SCN} | 2161.5 (0.2) | 12.3 (0.5) | −0.1 | 0.1 | −0.6 | −0.8 | 1.1 | −0.2 |
| M30C _{SCN} | 2159.6 (0.2) | 12.7 (0.3) | <i>b</i> | <i>b</i> | <i>b</i> | <i>b</i> | <i>b</i> | <i>b</i> |
| Y31C _{SCN} | 2161.1 (0.1) | 14.1 (0.4) | −0.9 | 1.3 | −2.6 | 0.3 | −0.4 | −2.7 |
| K32C _{SCN} | 2159.2 (0.1) | 13.4 (0.2) | 1.3 | −1.9 | −1.6 | 0.9 | −1.3 | −2.5 |
| S33C _{SCN} | 2161.2 (0.1) | 13.6 (0.7) | 0.1 | −0.1 | −1.8 | 0.4 | −0.6 | −2.9 |
| K52C _{SCN} | 2160.5 (0.1) | 12.1 (0.3) | <i>b</i> | <i>b</i> | <i>b</i> | <i>b</i> | <i>b</i> | <i>b</i> |
| N54C _{SCN} | 2162.2 (0.1) | 11.6 (0.4) | −1.3 | 1.9 | −0.5 | −0.7 | 1.0 | 0.0 |

^a Reported errors are one standard deviation of multiple experiments. ^b Docked complex did not form.

two residues, I18C_{SCN} and R20C_{SCN}, each displayed a vibrational frequency of 2163.1 cm⁻¹, 0.5 cm⁻¹ higher in energy than free MeSCN in the same buffer and collected under the same conditions, this hypothesis would conclude that these two residues are *more* solvent-exposed than free MeSCN in buffer. Under this interpretation, vibrational frequencies lower than 2162.6 cm⁻¹ in our experiments therefore indicate that the protein secondary or tertiary structure screens the side chain from full exposure to water. This scale suggests that the residues G28C_{SCN}, M30C_{SCN}, and K32C_{SCN}, with the lowest observed vibrational frequencies of ~2159.5 cm⁻¹, are in the most hydrophobic environment on the Ralβ surface.

These two hypotheses directly contradict one another; the first hypothesis supposes that solvent exposure corresponds to low measured absorption energy, and the second supposes that solvent exposure corresponds to high measured absorption energy. There are several possible sources for this contradiction, primarily that the observed correlation between SASA and thiocyanate vibrational frequency is rather weak and that the differences in absorption energy from the most solvent-exposed to the most solvent-excluded thiocyanate is rather small (4 cm⁻¹). It is also possible that both previous experiments and the results reported here actually reflect specific protein-dependent Stark shifts which have not yet been identified. Finally, it is also worth noting the complex nature of a protein–water interface, where both hydrophilic and hydrophobic amino acid side chains are exposed to the boundary between the low (protein) and high (water) dielectric media. The protein and its surface hydration layer constitute a chemically, structurally, and electrostatically complex environment that must be examined with physically appropriate high-level calculations.^{107–110} In particular, the nitrile moiety of the thiocyanate probe is a weak hydrogen bond acceptor both by the nitrogen atom (parallel to the nitrile bond axis) and by the π -cloud of the triple bond between the C and N.⁶¹ The response of the nitrile vibrational probe to the electrostatic-field-created protein–water interface is clearly more complex than just sequestration of the side chain from water and can be observed only with high-resolution measurements. Our results indicate that the absorption energy of the thiocyanate probe inserted at protein surface amino acid residues correlates qualitatively to subtle changes in solvent-exposed surface area, but the exact nature of the response to aqueous environment must be explored with extensive modeling of the protein–thiocyanate–water interaction.^{111,112}

C. Electrostatic Calculations of SCN-Labeled Ralβ Monomers. As shown in Figure 8, calculations of the electric field using PB do not correlate with the measured absorption energy of SCN-labeled Ralβ mutants ($r^2 = 0.0284$). Furthermore, the experimental fwhm should correlate to the standard deviation of calculated field as derived from the Boltzmann distribution because the width of the vibrational absorption is a function of structural variability of the nitrile in its environment. However, there is a slight *negative* correlation between the standard deviation of the electrostatic field calculation and the measured fwhm (described below) of the vibrational absorption ($r^2 = 0.255$, slope = $-3.97 \text{ cm } k_B T e^{-1} \text{ Å}^{-1}$, data not shown), meaning that the variability of calculated fields tended to decrease as the experimentally measured fwhm increased. This nonphysical result further highlights the challenges of predicting electrostatic fields at the complex protein–water interface. Our naïve Coulomb calculation of electric field from atomic point charges yielded qualitatively the same results as the PB solution with regard to field and standard deviation of field (data not shown).

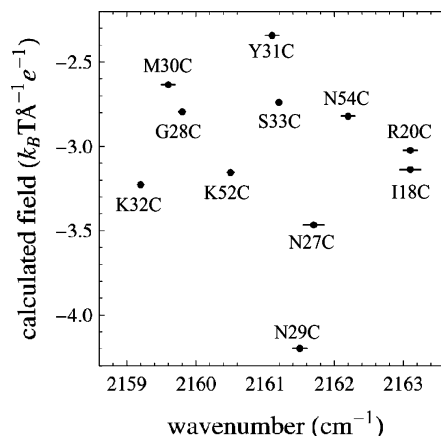


Figure 8. Boltzmann-weighted electric field versus measured absorption energy for the Ralβ mutants. Horizontal lines reflect the experimental uncertainty shown in Figure 6. The electric field was calculated from the slope of the Poisson–Boltzmann solution at the nitrile bond midpoint. The nitrile charges were set to zero for this calculation (see text). The calculated electric fields do not correlate with the measured absorption energy ($r^2 = 0.0284$).

These results should not be taken as a failure of PB per se, but rather, emphasize the difficulty of attempting to calculate the electrostatics of biomolecules in an attempt to make a comparison with experimental results. It is possible that a solvent reaction field approach using PB would be more reliable than the single-point Poisson–Boltzmann calculation we have described here, since grid-based PB solvers such as APBS should have large errors near charge centers.¹¹³ In this approach, the full potential would be the sum of the potential due to partial charges in a low dielectric plus the difference in potential with and without a dielectric boundary (the reaction field). We have attempted to address the issue of proximate charge centers by ignoring the nitrile charges, which have a constant contribution to the total potential. Under this approximation, our fields are derived from a calculated potential ~1.5 bond lengths away from the nearest charge center. This has clearly failed to yield adequate results, and for this reason, we are currently exploring the effect of protein dielectric constant, grid size, and spacing; attempting PB-based reaction field calculations; critically examining our sampling procedures; considering the use of polarizable force fields in PB calculations;^{114,115} and reviewing the theoretical basis for the vibrational Stark effect to learn how to calculate fields with PB that agree with our VSE measurements. We are also exploring more sophisticated calculation methods, such as calculating our experimental vibrational spectra from electron densities derived from density functional theory, but such methods are necessarily more computationally intense than PB. For this reason, our further work will also assess the reliability of fast, inexpensive PB solutions to interpret the results of VSE measurements and guide the design of future VSE experiments.

The Rap–Raf interaction has been studied by the protein dipoles Langevin dipoles (PDL) model in combination with the linear response approximation, which accounts for physical effects much more accurately than PB approaches.⁴⁰ This work addressed the contributions to the free energy of binding not only due to different physical considerations but also the contributions of particular amino acids on both Rap and Raf. This detailed investigation was similar to what we were trying to measure, but we have refrained from direct comparison for two reasons. First, crystal structures show that Raf binds in a slightly different manner to Ras and Rap, compared to Ral, and

TABLE 3: Binding Kinetics of WT Ral and SCN-Labeled Ral β Mutants Docked to WT Ras and WT Rap^a

| Ral β mutation | WT Ras (μ M) | WT Rap (μ M) |
|----------------------|-------------------|-------------------|
| WT | 2.7 (0.2) | 0.18 (0.01) |
| I18C _{SCN} | 3.5 (0.5) | 0.13 (0.01) |
| R20C _{SCN} | 3.9 (0.1) | 0.23 (0.02) |
| N27C _{SCN} | 0.72 (0.03) | 0.12 (0.02) |
| G28C _{SCN} | 2.6 (0.6) | 0.16 (0.02) |
| N29C _{SCN} | 3.2 (0.4) | 0.24 (0.02) |
| Y31C _{SCN} | 3.4 (0.3) | 0.27 (0.03) |
| K32C _{SCN} | 0.75 (0.04) | 0.14 (0.02) |
| S33C _{SCN} | 1.4 (0.3) | 0.23 (0.02) |
| N54C _{SCN} | 2.1 (0.1) | 0.25 (0.02) |

^a K_d values were obtained by fitting the k_{obs} from the GDI assay to eq 1. Errors represent one standard deviation from multiple experiments.

full exploration of electrostatic probes on Raf has only recently begun in our laboratory. Second, these calculations were of free energies, not spatially resolved electrostatic potentials, which would be directly comparable to VSE measurements. We are hopeful that these sophisticated and high-level calculations can be applied to the experimental observable that we report here, measured local electrostatic field. Comparable experiments using Raf to carry the thiocyanate probe are currently underway in our laboratory, which will allow us to connect experimental VSE spectroscopic measurements, experimental free energy of binding, and high-level PDL calculations in a single protein–protein interface. This will be a significant advance in this field.

D. VSE Spectroscopy of the Docked Protein–Protein Complex. Thiocyanate-labeled Ral β mutants were incubated with either WT Ras or WT Rap, and the absorption energy of the nitrile probe was measured and compared with the monomeric Ral β protein. Figure 5 shows a representative example of Ral β G28C_{SCN} interacting with both GTPases. When docked to WT Ras, the absorption peak of the nitrile label increased in frequency by 1.8 cm⁻¹. This corresponds to a measured $\Delta\bar{F}_{dock}$ of -2.6 MV/cm for the docked complex versus monomeric Ral β G28C_{SCN}. When incubated with Rap, the thiocyanate vibrational frequency of Ral β G28C_{SCN} increased by 2.2 cm⁻¹, indicating a change in the electrostatic field experienced by the probe of -3.1 MV/cm. These two values of $\Delta\bar{F}_{dock}$ demonstrate that the thiocyanate probe experiences a slightly different electrostatic field when it is immersed in the Ras interface as compared to the Rap interface. Figure 5 also shows that the full width at half-maximum (fwhm) of the thiocyanate frequency decreased upon docking with both species, shrinking by 2.5 and 2.3 cm⁻¹ for docking with Ras and Rap, respectively, compared with the solvent-exposed monomeric structure.

Interpretation of all VSE spectra presented here depends on the Ras-effector interface forming without any substantial deviations from the Ras-RalGDS crystal structure shown in Figure 2.⁷⁵ Formation of the interface may be perturbed by the extensive mutation required to make the SCN-labeled Ral β mutants: mutation to alanine of the wild-type cysteine residues at positions 16 and 17 and introduction of the thiocyanate functional group at the protein–protein interface. The formation of the docked complex was verified by gel filtration chromatography and K_d measurements. The SCN-labeled Ral β mutants G28C_{SCN} and N54C_{SCN} as well as WT RalGDS were incubated with either WT Ras or WT Rap. Gel filtration chromatography of this solution resulted in the clear elution of the docked complex at ~30 kDa, consistent with the docked complex. Table 3 summarizes K_d measurements of labeled Ral β mutants and RalGDS binding to WT Ras and WT Rap. The WT Ras-WT

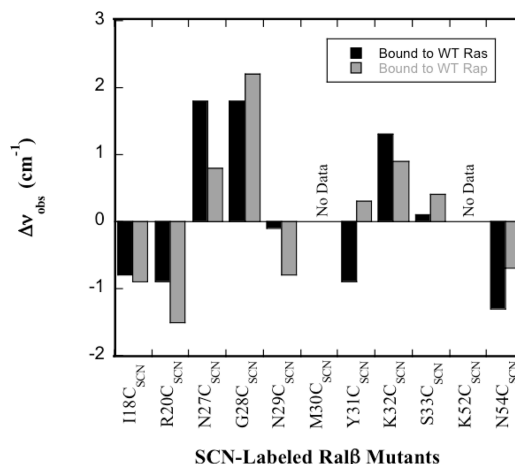


Figure 9. Change in absorption energy, Δv_{obs} , of a nitrile probe on SCN-labeled Ral β mutants when bound to WT Ras (black) or WT Rap (gray), where $\Delta v_{obs} = 0$ represents no change from the thiocyanate absorption energy in labeling buffer reported in Figure 6.

RalGDS complex formed with a K_d of $2.7 \pm 0.2 \mu$ M, and the WT Ras-Ral β -SCN complexes displayed K_d 's ranging from 0.75 to 3.9 μ M. The WT Rap-WT RalGDS complex formed with $K_d = 0.18 \pm 0.01 \mu$ M, and the SCN-labeled Ral β mutants docked to WT Rap with K_d 's ranging from 0.12 to 0.27 μ M. Indeed, several SCN-labeled Ral β mutants exhibited a lower K_d than the wild-type complex. On the basis of these results, we conclude that mutation and thiocyanate probe incorporation do not interfere with the formation of the docked complex.

Furthermore, the full width at half-maximum (fwhm) of the thiocyanate absorbance (listed in Table 2) usually decreased on binding, sometimes by as much as 3 cm⁻¹. This indicates that the thiocyanate probe has been confined to a more compact environment, where it experiences less conformational flexibility on the cyanocysteine side chain. This empirical result has been observed before.³⁹ Taken together, the gel filtration, the kinetic evidence, and the spectroscopic line widths verify formation of the docked complex. Extensive molecular dynamics simulations of the docked protein–protein complexes currently underway in our laboratory will further interrogate the position of the thiocyanate functional group within the protein–protein interface.

Formation of a binary docked complex between SCN-labeled Ral β mutants and WT Ras or WT Rap led to a change in electrostatic environment near the probe molecule relative to the solvent-exposed condition. Changes in the nitrile absorption energy (Δv_{obs}) due to binding are summarized in Figure 9 and Table 2 ($\Delta v_{obs} = 0$ represents no change from the thiocyanate absorption energy in labeling buffer shown in Figure 6). These shifts are related to electrostatic field through the known value of the Stark tuning rate, $\Delta\bar{\mu}_{SCN}$, of 0.7 cm⁻¹/(MV/cm); the calculated $\Delta\bar{F}_{dock}$ are reported in Table 2. Docking experiments for the mutants Ral β M30C_{SCN} and Ral β K52C_{SCN} have not yet been successful; we have observed extensive precipitation when the labeled Ral β mutant is incubated with Ras or Rap under these conditions.

The complex nature of electrostatic fields upon forming the docked Ras-Ral β or Rap-Ral β complex is revealed in Figure 9. In locations where the nitrile probe experiences a negative change in absorption energy (and, thus, positive $\Delta\bar{F}_{dock}$), the magnitude of the energy shift is usually small (<1 cm⁻¹), such as seen with Ral β I18C_{SCN}, R20C_{SCN}, N29C_{SCN}, and N54C_{SCN}. However, for N27C_{SCN}, G28C_{SCN}, and K32C_{SCN}, the shift in absorption energy is always to higher energy and large, up to

2.2 cm⁻¹ for Ral β G28C_{SCN} binding to WT Rap. This represents a large negative $\Delta\bar{F}_{\text{dock}}$ (up to -3.1 MV/cm for Ral β G28C_{SCN} binding to WT Rap) that the thiocyanate experiences upon being moved from the largely solvent-exposed surface to the docked interface. These large shifts may indicate regions of the interface near N27, G28, and K32 that are important for protein recognition.

A central problem in the formation of any protein–protein interface is how a protein distinguishes an appropriate downstream effector from other biomolecules encountered in the crowded environment of the cellular milieu. Because of the structural similarity of Ras and Rap (Figure 1) and the structural similarity of the docked protein–protein complexes, it is plausible that Ras and Rap share a basic functional mechanism in the manner by which they recognize their effectors at Switch I.⁶⁹ Five of the nine SCN-labeled Ral β mutants that we have docked to WT Ras and WT Rap (I18C_{SCN}, R20C_{SCN}, G28C_{SCN}, K32C_{SCN}, and S33C_{SCN}) display similar changes in electrostatic field when bound to both GTPases. Two of these residues, R20 and K32, are known to be conserved across all Ras binding domains.^{75,116} (Unfortunately, we have not yet been able to measure changes in electrostatic field at K52, another conserved residue, upon formation of the docked complexes.) The similar electrostatic environment experienced by R20 and K32 in the docked complex is evidence that these residues are key to recognition by the Switch I region of Ras-like GTPases. We are currently investigating the importance of these residues to the favorable binding free energy of RalGDS to both Ras and Rap.

In addition, the data in Figure 9 point to regions of the interface that could direct the specificity of RalGDS for Ras *as opposed to* Rap. Residues N27C_{SCN}, N29C_{SCN}, Y31C_{SCN}, and N54C_{SCN} have dramatically different changes in absorption energy when docked with the two different proteins. This is particularly interesting in the case of the thiocyanate on N54C_{SCN}. In the docked Ras-RalGDS complex, RalGDS N54 is ~ 3.5 Å away from Ras E31, whereas Rap has a lysine at this position. This residue has been the focus of experiments to test its importance in differentiating the Ras binding surface from that of Rap. For example, although Raf is the native effector of Ras, a crystal structure of the mutant Ras E31K bound to RalGDS has been characterized.⁷⁵ This is not a structural effect; the backbone rmsd of pdb 1LFD (RasE31K) compared with 3LBH (WT Ras)¹¹⁷ is ~ 0.5 Å, indicating that the mutation Ras E31K does not introduce conformational changes in the Switch I region, which would account for this preference in binding partners. On the other hand, a crystal structure of Rap K31E bound to the RBD of Raf has been solved.⁷⁷ The crystallography data support the hypothesis that this residue is responsible for enabling the GTPase to discriminate downstream effectors it encounters.⁷⁶ Thus, the discrimination of Ras/Rap to Raf/RalGDS appears to be due to electrostatic effects and, thus, directly measurable with VSE spectroscopy. Investigation of the role of electrostatic field at position 31 of the GTPase through VSE spectroscopy with thiocyanate labels on Ral β mutants is currently underway in our laboratory.

Although initial electric field calculations do not appear to correlate to experimentally observed vibrational frequencies, it is still possible that through cancellations of errors, calculations will be more successful in predicting the observed shifts due to binding. Molecular dynamics simulations of the nine docked complexes to estimate the probe torsional free energy surface are currently underway in our laboratory. These results will be reported in subsequent publications.

Conclusions

This is the first report of a comprehensive experimental map of electrostatic fields at any protein–protein interface. Systematic incorporation of the nitrile VSE probe throughout two structurally similar interfaces has demonstrated the complexity of the electrostatic environment in a stable docked complex. The consequences of electrostatic field on functional questions of interface formation are the focus of current work in our laboratory. Moreover, these data provide a comprehensive benchmark to judge the efficacy of structural and computational methods to simulate the structural landscape and electrostatic environment of a complex protein–protein interface. In particular, they provide experimental data for comparison of electrostatic calculation methods used in the literature to predict electrostatic fields at protein–protein interfaces. This work is currently underway and will be reported in future publications.

Acknowledgment. This work was supported by the Burroughs Wellcome Fund (1007207.01) and The Welch Foundation (F-1722). L.J.W. holds a Career Award at the Scientific Interface from the Burroughs Wellcome Fund. The authors acknowledge the Texas Advanced Computing Center (TACC) at The University of Texas at Austin for providing high-performance computing resources that have contributed to the results reported within this paper.

References and Notes

- (1) Camacho, C. J.; Kimura, S. R.; DeLisi, C.; Vajda, S. *Biophys. J.* **2000**, *78*, 1094–1105.
- (2) Camacho, C. J.; Vajda, S. *Proc. Natl. Acad. Sci.* **2001**, *98*, 10636–10641.
- (3) Camacho, C. J.; Weng, Z.; Vajda, S.; DeLisi, C. *Biophys. J.* **1999**, *76*, 1166–1178.
- (4) Dastidar, S. G.; Madhumalar, A.; Fuentes, G.; Lane, D. P.; Verma, C. S. *Theor. Chem. Acc.* **2010**, *125*, 621–635.
- (5) Gromiha, M. M.; Yokota, K.; Fukui, K. *Int. J. Biol. Macromol.* **2010**, *46*, 187–192.
- (6) Panjkovich, A.; Aloy, P. *Mol. BioSyst.* **2010**, *6*, 741–749.
- (7) Pons, C.; Grosdidier, S.; Solernou, A.; Perez-Cano, L.; Fernandez-Rrecio, J. *Proteins* **2010**, *78*, 95–108.
- (8) Rajamani, D.; Thiel, S.; Vajda, S.; Camacho, C. J. *Proc. Natl. Acad. Sci.* **2004**, *101*, 11287–11292.
- (9) Bader, G. D.; Donaldson, I.; Wolting, C.; Ouellette, B. F. F.; Pawson, T.; Hogue, C. W. V. *Nucleic Acids Res.* **2001**, *29*.
- (10) Blommers, M. J. J.; Strauss, A.; Geiser, M.; Ramage, P.; Sparrer, H.; Jahnke, W. *Top. Curr. Chem.* **2008**, *273*, 1–14.
- (11) Bonet, J.; Caltabiano, G.; Khan, A. K.; Johnston, M. S.; Corbi, C.; Gomez, A.; Rovira, X.; Teyra, J.; Villa-Freixa, J. *Proteins* **2006**, *63*, 65–77.
- (12) Enright, A. J.; Iliopoulos, I.; Kyrpides, N. C.; Ouzounis, C. A. *Nature* **1999**, *402*, 86–90.
- (13) Glaser, F.; Steinberg, D. M.; Vakser, I. A.; Ben-Tal, N. *Proteins: Struct. Funct. Genet.* **2001**, *43*, 89–102.
- (14) Jones, S.; Thornton, J. M. *Proc. Natl. Acad. Sci.* **1996**, *93*, 13–20.
- (15) Keskin, O.; Ma, B.; Rogale, K.; Gunasekaran, K.; Nussinov, R. *Phys. Biol.* **2005**, *2*, S24–S35.
- (16) Lo Conte, L.; Chothia, C.; Janin, J. *J. Mol. Biol.* **1999**, *2385*, 2177–2198.
- (17) McCoy, A. J.; Epa, V. C.; Colman, P. M. *J. Mol. Biol.* **1997**, *268*, 570–584.
- (18) Nooren, I. M. A.; Thornton, J. M. *EMBO J.* **2003**, *22*, 3486–3492.
- (19) Norel, R.; Petrey, D.; Wolfson, H. J.; Nussinov, R. *Proteins* **1999**, *36*, 307–317.
- (20) Wodak, S. J.; Janin, J. *Adv. Protein Chem.* **2003**, *61*, 9–73.
- (21) Xenarios, I.; Rice, D. W.; Salwinski, L.; Baron, M. K.; Marcotte, E. M.; Eisenberg, D. *Nucleic Acids Res.* **2000**, *28*, 289–291.
- (22) Gunner, M. R.; Nicholls, A.; Honig, B. *J. Phys. Chem.* **1996**, *100*, 4277–4291.
- (23) Honig, B.; Nicholls, A. *Science* **1995**, *268*, 1144–1149.
- (24) Lee, L. P.; Tidor, B. *Protein Sci.* **2001**, *10*, 362–377.
- (25) Simonson, T. *Curr. Opin. Struct. Biol.* **2001**, *11*, 243–252.
- (26) Villa, J.; Warshel, A. *J. Phys. Chem. B* **2001**, *105*, 7887–7907.

- (27) Warshel, A.; Papazyan, A. *Curr. Opin. Struct. Biol.* **1998**, *8*, 211–217.
- (28) Baran, K. L.; Chimenti, M. S.; Schlessman, J. L.; Fitch, C. A.; Herbst, K. J.; Garcia-Moreno, B. E. *J. Mol. Biol.* **2008**, *379*, 1045–1062.
- (29) Castaneda, C. A.; Fitch, C. A.; Majumdar, A.; Khangulov, V.; Schlessman, J. L.; Garcia-Moreno, B. E. *Proteins* **2009**, *77*, 570–588.
- (30) Danielson, M. A.; Falke, J. J. *Annu. Rev. Biophys. Biomol. Struct.* **1996**, *25*, 163–195.
- (31) Forsyth, W. R.; Antosiewicz, J. M.; Robertson, A. D. *Proteins* **2002**, *48*, 388–403.
- (32) Harms, M. J.; Castaneda, C. A.; Schlessman, J. L.; Sue, G. R.; Isom, D. G.; Cannon, B. R.; Garcia-Moreno, B. E. *J. Mol. Biol.* **2009**, *389*, 34–47.
- (33) Matousek, W. M.; Ciani, B.; Fitch, C. A.; Garcia-Moreno, B. E.; Kammerer, R. A.; Alexandrescu, A. T. *J. Mol. Biol.* **2007**, *374*, 206–219.
- (34) Pearson, J. G.; Oldfield, E.; Lee, F. S.; Warshel, A. *J. Am. Chem. Soc.* **1993**, *115*, 6851–6862.
- (35) Schutz, C. N.; Warshel, A. *Proteins* **2001**, *44*, 400–417.
- (36) Thurlkill, R. L.; Grimsley, G. R.; Scholtz, J. M.; Pace, C. N. *J. Mol. Biol.* **2006**, *362*, 594–604.
- (37) Meng, Y.; Roitberg, A. E. *J. Chem. Theory Comput.* **2010**, *6*, 1401–1412.
- (38) Suydam, I. T.; Snow, C. D.; Pande, V. S.; Boxer, S. G. *Science* **2006**, *313*, 200–204.
- (39) Webb, L. J.; Boxer, S. G. *Biochemistry* **2008**, *47*, 1588–1598.
- (40) Muegge, I.; Schweins, T.; Warshel, A. *Proteins* **1998**, *30*, 407–423.
- (41) Nielsen, J. E.; Andersen, K. V.; Honig, B.; Hooft, R. W. W.; Klebe, G.; Vriend, G.; Wade, R. C. *Protein Eng.* **1999**, *12*, 657–662.
- (42) Khandogin, J.; Brooks, C. L. *Biochemistry* **2006**, *45*, 9363–9373.
- (43) MacDermid, C. M.; Kaminski, G. A. *J. Phys. Chem. B* **2007**, *111*, 9036–9044.
- (44) Schubert, M.; Poon, D. K. Y.; Wicki, J.; Tarling, C. A.; Kwan, E. M.; Nielsen, J. E.; Withers, S. G.; McIntosh, L. P. *Biochemistry* **2007**, *46*, 7383–7395.
- (45) Warshel, A.; Sharma, P. K.; Kato, M.; Parson, W. W. *Biochim. Biophys. Acta* **2006**, *1764*, 1647–1676.
- (46) Andrews, S. S.; Boxer, S. G. *J. Phys. Chem. A* **2000**, *104*, 11853–11863.
- (47) Andrews, S. S.; Boxer, S. G. *J. Phys. Chem. A* **2002**, *106*, 469–477.
- (48) Fafarman, A. T.; Webb, L. J.; Chuang, J. I.; Boxer, S. G. *J. Am. Chem. Soc.* **2006**, *128*, 13356–13357.
- (49) Suydam, I. T.; Boxer, S. G. *Biochemistry* **2003**, *42*, 12050–12055.
- (50) Sigala, P. A.; Fafarman, A. T.; Bogard, P. E.; Boxer, S. G.; Herschlag, D. *J. Am. Chem. Soc.* **2007**, *129*, 12104–12105.
- (51) Aschaffenburg, D. J.; Moog, R. S. *J. Phys. Chem. B* **2009**, *113*, 12736–12743.
- (52) Edelstein, L.; Stetz, M. A.; McMahon, A.; Londergan, C. H. *J. Phys. Chem. B* **2010**, *114*, 4931–4936.
- (53) Getahun, Z.; Huang, C. Y.; Wang, T.; De Leon, B.; DeGrado, W. F.; Gai, F. *J. Am. Chem. Soc.* **2002**, *125*, 405–411.
- (54) Maienschein-Cline, M. G.; Londergan, C. H. *J. Phys. Chem. A* **2007**, *111*, 10010–10025.
- (55) Miyake-Stoner, S.; Miller, A. M.; Hammill, J. T.; Peeler, J. C.; Hess, K. R.; Mehl, R. A.; Brewer, S. H. *Biochemistry* **2009**, *48*, 5953–5962.
- (56) Schultz, K. C.; Supekova, L.; Ryu, Y.; Xie, J.; Perera, R.; Schultz, P. G. *J. Am. Chem. Soc.* **2006**, *128*, 13984–13985.
- (57) Taskent-Sezgin, H.; Chung, J.; Patsalo, V.; Miyake-Stoner, S.; Miller, A. M.; Brewer, S. H.; Mehl, R. A.; Green, D. F.; Raleigh, D. P.; Carrico, I. *Biochemistry* **2009**, *48*, 9040–9046.
- (58) Waagele, M. M.; Tucker, M. J.; Gai, F. *Chem. Phys. Lett.* **2009**, *478*, 249–253.
- (59) Krummel, A. T.; Zanni, M. T. *J. Phys. Chem. B* **2008**, *112*, 1336–1338.
- (60) Silverman, L. N.; Pitzer, M. E.; Ankomah, P. O.; Boxer, S. G.; Fenlon, E. E. *J. Phys. Chem. B* **2007**, *111*, 11611–11613.
- (61) Choi, J. H.; Oh, K. I.; Lee, H.; Lee, C.; Cho, M. *J. Chem. Phys.* **2008**, *128*, 134506.
- (62) Lindquist, B. A.; Corcelli, S. A. *J. Phys. Chem. B* **2008**, *112*, 6301–6303.
- (63) Lindquist, B. A.; Furse, K. E.; Corcelli, S. A. *Phys. Chem. Chem. Phys.* **2009**, *11*, 8119–8132.
- (64) Lindquist, B. A.; Haws, R. T.; Corcelli, S. A. *J. Phys. Chem. B* **2008**, *112*, 13991–14001.
- (65) Oh, K. I.; Choi, J. H.; Lee, J. H.; Han, J. B.; Lee, H.; Cho, M. *J. Chem. Phys.* **2008**, *128*, 154504.
- (66) Reimers, J. R.; Hall, L. E. *J. Am. Chem. Soc.* **1999**, *121*, 3730–3744.
- (67) Reimers, J. R.; Hush, N. S. *J. Phys. Chem. A* **1999**, *103*, 10580–10587.
- (68) Reimers, J. R.; Zeng, J.; Hush, N. S. *J. Phys. Chem.* **1996**, *100*, 1498–1504.
- (69) Krauss, G. *Biochemistry of Signal Transduction and Regulation*; 3rd ed.; Wiley-VCH Verlag: Weinheim, Germany, 2003.
- (70) Cox, A. D.; Der, C. J. *Oncogene* **2003**, *22*, 8999–9006.
- (71) Downward, J. *Nat. Cancer Rev.* **2002**, *3*, 11–22.
- (72) Repasky, G. A.; Chenette, E. J.; Der, C. J. *Trends Cell Biol.* **2004**, *14*, 639–647.
- (73) Shields, J. M.; Pruitt, K.; McFall, A.; Shaub, A.; Der, C. J. *Trends Cell Biol.* **2000**, *10*, 147–154.
- (74) Geyer, M.; Herrmann, C.; Wohlgenuth, S.; Wittinghofer, A.; Kalbitzer, H. R. *Nat. Struct. Biol.* **1997**, *4*, 694–699.
- (75) Huang, L.; Hofer, F.; Martin, G. S.; Kim, S. H. *Nat. Struct. Biol.* **1998**, *5*, 422–426.
- (76) Nassar, N.; Horn, G.; Herrmann, C.; Block, C.; Janknecht, R.; Wittinghofer, A. *Nat. Struct. Biol.* **1996**, *3*, 723–729.
- (77) Nassar, N.; Horn, G.; Herrmann, C.; Scherer, A.; McCormick, F.; Wittinghofer, A. *Nature* **1995**, *375*, 554–560.
- (78) Pai, E. F.; Kregel, U.; Petsko, G. A.; Goody, R. S.; Kabsch, W.; Wittinghofer, A. *EMBO J.* **1990**, *9*, 2351–2359.
- (79) Herrmann, C. *Curr. Opin. Struct. Biol.* **2003**, *13*, 122–129.
- (80) Herrmann, C.; Horn, G.; Spaargaren, M.; Wittinghofer, A. *J. Biol. Chem.* **1996**, *271*, 6794–6800.
- (81) Rudolph, M. G.; Linnemann, T.; Grunewald, P.; Wittinghofer, A.; Vetter, I. R.; Herrmann, C. *J. Biol. Chem.* **2001**, *276*, 23914–23921.
- (82) Mott, H. R.; Carpenter, J. W.; Zhong, S.; Ghosh, S.; Bell, R. M.; Campbell, S. L. *Proc. Natl. Acad. Sci.* **1996**, *93*, 8312–8317.
- (83) Sprang, S. R. *Annu. Rev. Biochem.* **1997**, *66*, 639–678.
- (84) Takai, Y.; Sasaki, T.; Matozaki, T. *Physiol. Rev.* **2001**, *81*, 153–208.
- (85) Kapust, R. B.; Tozser, J.; Fox, J. D.; Anderson, D. E.; Cherry, S.; Copeland, T. D.; Waugh, D. S. *Protein Eng.* **2001**, *14*, 993–1000.
- (86) Boriack-Sjodin, P. A.; Margarit, S. M.; Bar-Sagi, D.; Kuriyan, J. *Nature* **1998**, *394*, 337–343.
- (87) Russell, R. B.; Barton, G. J. *Proteins: Struct. Funct. Genet.* **1992**, *14*, 309–323.
- (88) Humphrey, W.; Dalke, A.; Schulten, K. *J. Mol. Graphics* **1996**, *14*, 33–38.
- (89) http://avogadro.openmolecules.net/wiki/Main_Page (accessed Apr 1, 2010).
- (90) Case, D. A.; Darden, T. A.; Cheatham, T. E.; Simmerling, C. L.; Wang, J.; Duke, R. E.; Luo, R.; Walker, R. C.; Zhang, W.; Merz, K. M.; Roberts, B. P.; Wang, B.; Hayik, S.; Roitberg, A. E.; Seabra, G.; Kolossvy, I.; Wong, K. F.; Paesani, F.; Vanicek, J.; Wu, X.; Brozell, S. R.; Steinbrecher, T.; Gohlke, H.; Cai, Q.; Ye, X.; Wang, J.; Hsieh, M. J.; Cui, G.; Roe, D. R.; Mathews, D. H.; Seetin, M. G.; Sagui, C.; Babin, V.; Luchko, T.; Gusarov, S.; Kovalenko, A.; Kollman, P. A. *AMBER 11*; University of California, San Francisco, 2010.
- (91) van der Spoel, D.; Lindahl, E.; Hess, B.; Groenhof, G.; Mark, A. E.; Berendsen, H. J. C. *J. Comput. Chem.* **2005**, *26*, 1701–1718.
- (92) Duan, Y.; Wu, C.; Chowdhury, S.; Lee, M. C.; Xiong, G.; Zhang, W.; Yang, R.; Cieplak, P.; Luo, R.; Lee, T.; Caldwell, J. W.; Wang, J.; Kollman, P. A. *J. Comput. Chem.* **2003**, *24*, 1999–2012.
- (93) Sorin, E. J.; Pande, V. S. *Biophys. J.* **2005**, *88*, 2472–2493.
- (94) Kharitonov, Y. Y.; Knyazeva, N. A. *Izvestiya Akademii Nauk SSSR-Seriya Khimicheskaya* **1971**, *11*, 2329–2334.
- (95) Gordon, M. S.; Schmidt, M. W. *Theory and Applications of Computational Chemistry, the First Forty Years*; Elsevier: Amsterdam, 2005, pp 1167–1189.
- (96) Schmidt, M. W.; Baldrige, K. K.; Boatz, J. A.; Elbert, S. T.; Gordon, M. S.; Jensen, J. J.; Koseki, S.; Matsunaga, N.; Nguyen, K. A.; Su, S.; Windus, T. L.; Dupuis, M.; Montgomery, J. A. *J. Comput. Chem.* **1993**, *14*, 1347–1363.
- (97) Cieplak, P.; Cornell, W. D.; Bayly, C.; Kollman, P. A. *J. Comput. Chem.* **1995**, *16*, 1357–1377.
- (98) Mahoney, M. W.; Jorgensen, W. L. *J. Chem. Phys.* **2000**, *2000*, 8910–8922.
- (99) Darden, T.; York, D.; Pedersen, L. G. *J. Chem. Phys.* **1993**, *98*, 10089–10092.
- (100) Essmann, U.; Perera, L.; Berkowitz, M. L.; Darden, T.; Lee, H.; Pedersen, L. G. *J. Chem. Phys.* **1995**, *103*, 8577–8593.
- (101) Ryckaert, J. P.; Ciccotti, G.; Berendsen, H. J. C. *J. Comput. Phys.* **1977**, *23*, 327–341.
- (102) Miyamoto, S.; Kollman, P. A. *J. Comput. Chem.* **1992**, *13*, 952–962.
- (103) Gallicchio, E.; Andrec, M.; Felts, A. K.; Levy, R. M. *J. Phys. Chem. B* **2005**, *109*, 6722–6731.
- (104) Roux, B. *Comput. Phys. Commun.* **1995**, *91*, 275–282.
- (105) Baker, N. A.; Sept, D.; Joseph, S.; Holst, M. J.; McCammon, J. A. *Proc. Natl. Acad. Sci.* **2001**, *98*, 10037–10041.
- (106) Mukherjee, S.; Chowdhury, P.; DeGrado, W. F.; Gai, F. *Langmuir* **2007**, *23*, 11174–11179.
- (107) Bagchi, B. *Chem. Rev.* **2005**, *105*, 3197–3219.

- (108) Bellissent-Funel, M. C. *J. Mol. Liq.* **2000**, *84*, 39–52.
- (109) Bizzarri, A. R.; Cannistraro, S. *J. Phys. Chem. B* **2002**, *106*, 6617–6633.
- (110) Johnson, M. E.; Malardier-Jugroot, C.; Murarka, R. K.; Head-Gordon, T. *J. Phys. Chem. B* **2009**, *113*, 4082–4092.
- (111) King, G.; Lee, F. S.; Warshel, A. *J. Chem. Phys.* **1991**, *95*, 4366–4377.
- (112) Warshel, A.; Levitt, M. *J. Mol. Biol.* **1976**, *103*, 227–249.
- (113) Cerutti, D. S.; Baker, N. A.; McCammon, J. A. *J. Chem. Phys.* **2007**, *127*, 10.1063/1.2771171-1-28.
- (114) Ponder, J. W.; Wu, C.; Ren, P.; Pande, V. S.; Chodera, J. D.; Schnieders, M. J.; Haque, I.; Mobley, D. L.; Lambrecht, D. S.; DiStasio, R. A.; Head-Gordon, M.; Clark, G. N. I.; Johnson, M. E.; Head-Gordon, T. *J. Phys. Chem. B* **2010**, *114*, 2549–2564.
- (115) Warshel, A.; Kato, M.; Pisiakov, A. V. *J. Chem. Theory Comput.* **2007**, *3*, 2034–2045.
- (116) Ponting, C. P.; Benjamin, D. R. *Trends Biochem. Sci.* **1996**, *21*, 422–425.
- (117) Buhrman, G.; Holzapfel, G.; Fetters, S.; Mattos, C. *Proc. Natl. Acad. Sci.* **2010**, *107*, 4931–4936.

JP106974E